A hybrid physics-informed neural network for predicting fatigue life of axially loaded grouted connections for offshore wind turbine structures

Siyu ZHAO[1,2], *Zhenyu HUANG*[1]*, *Yingwu ZHOU*[1], *Feng XING*[3], *Xiaonan Hou*[2], *Jianqiao YE*[2]
1 Guangdong Provincial Key Laboratory of Durability for Marine Civil Engineering, Shenzhen University, Shenzhen, 518060, China
2 School of Engineering, Lancaster University, Lancaster LA1 4YR, UK
3 School of Mechanics and Construction Engineering, Jinan University, Guangzhou, 510632, China

Abstract

As a critical component of an offshore wind turbine foundation, grouted connections are susceptible to fatigue failure under long-term loading conditions, which makes the assessment of their fatigue behaviour essential for the overall structural integrity and maintenance. Compared to costly experimental characterization and computationally expensive numerical modelling, there is a high demand for developing a fast, efficient and accurate surrogate model to predict fatigue life. This paper develops a novel hybrid Physics-Informed Neural Network (PINN) model that integrates both simplified physical constraints and hidden physical laws to predict the fatigue life of axially loaded grouted connections, where the physical knowledge is the relationship between fatigue life and fatigue-related parameters. The results show that the developed hybrid PINN model achieves superior prediction accuracy compared to the current codes of practice, the conventional Deep Neural Network (DNN) model, the PINN model integrating simplified physical constraints (S-PINN), and the PINN model integrating hidden physical laws (H-PINN). To enhance the interpretability of the model, Shapley Additive Explanations (SHAP) analysis and physical consistency analysis are conducted to assess the contribution of each feature to the fatigue life and to investigate the distribution of predictions with respect to physical consistency. It's found that the new hybrid PINN model produces predictions that exhibit a higher degree of physical consistency than the purely data-driven DNN model, demonstrating the reliability and robustness of the model.

Keywords: Machine learning; Physics-informed neural network; Grouted connections; Fatigue life; Model interpretability.

1. Introduction

Grouted connections have been widely used in offshore wind turbines construction to connect the upper structure to the foundation, as shown in the monopiles, tripod structures, and jacket structures (Fig. 1) [1-4]. The high-strength grout between steel tubes at the connections can effectively resist the cyclic loads caused by the marine environment. However, the long-term exposure to environmental loading of winds, waves, and tides makes grouted connections susceptible to issues related to fatigue crack propagation and marine-induced erosion. This study focuses on the prediction of the fatigue life of axially loaded grouted connections, providing essential insights into structural safety and operational reliability.

The fatigue performance of grouted connections has been extensively investigated through both experimental tests and Finite Element Analysis (FEA). A key early contribution was made by Billington et al. [5] in 1980, who pioneered the use of tension-compression cyclic loading tests to establish a logarithmic linear relationship between the stress range and the fatigue life. Boswell et al. [6] further investigated the fatigue performance of grouted connections with shear keys through a series of fatigue tests under fully reversed cyclic loading conditions and concluded that higher strength grout demonstrated inferior fatigue performance than lower strength grout. In engineering applications, over the last few decades, the compressive strength of grouting materials has improved from 10-80 MPa to 140-170 MPa [7-10], with a strength up to 210 MPa being employed in underwater repair scenarios [9-10]. Despite these advancements, the criteria for selecting appropriate grout strength in engineering applications have not been clarified [4], and the influence of other key parameters, such as connection details and loading conditions, on fatigue performance remains insufficiently understood.

To address these limitations, Chen et al. [11] tested five cylindrical grouted connections with shear keys under a constant range of cyclic bending moments and found that the specimens that could endure 2 million load cycles without significant loss of bending capacity exhibited a reduced fatigue life of 1.28 million cycles due to the welding quality of the steel structures. Schaumann et al. [12] conducted nonlinear finite element analysis on local degradation and vertical misalignments of grouted connections and demonstrated that highly flexible structures could induce grout cracking and relative sliding at the interface, which resulted in abrasion and wear, thereby reducing fatigue life. Sørensen et al. [13] and Schaumann et al. [14] studied the fatigue performance of grouted connections in both dry and wet environments. The results showed that the interface slippage and grout degradation in the submerged environment accelerated the structural performance deterioration. The wear rate can be 2-18 times higher than that of grouted connections in the dry environment [15]. Johansen et al. [16] investigated the cyclic capacity of axially loaded grouted connections and found that the cyclic capacity was significantly lower than the static strength, and that the axial load level was a key factor influencing the fatigue performance of the structure. The design codes DNV-ST-0126 [17] and ISO 19902 [18] provide three-segment and single-segment logarithmic S-N curves, respectively, under pulsating and alternating loading conditions. Although the influence of the fatigue limit is not considered, these codes offer essential guidance for the fatigue design of grouted connections.

It may be concluded that previous tests in the literature were conducted as independent evaluations, with limited experimental data and large variations in choosing design parameters [19-20]. However, carrying out full-scale experiments are costly, time-consuming and it is difficult to simulate realistic environmental and loading conditions. Empirical formulas and FEA are unable to fully account for the nonlinear behaviour of the structures under complex loading conditions [21-22]. Given these limitations, machine learning approaches offer promising alternatives for fatigue performance evaluation, leveraging existing datasets from experimental and numerical sources.

Machine learning technology has demonstrated strong capability in extracting nonlinear relationships between input features and output features across different subject domains [23-25]. Among these applications, fatigue prediction has emerged as a promising area of research. Liu et al. [26] proposed a modified parameter-optimized support vector machine (SVM) model to predict the fatigue life of vibration isolation rubbers, which outperformed the back propagation neural network (BPNN) regression model with high efficiency and greater accuracy. Wang et al. [27] developed a novel machine learning approach by combining the Gray Wolf Optimization (GWO) algorithm with the XGBoost model for the fatigue life prediction of high-strength steel wires, and demonstrated the model’s generalization capability on wire specifications that are not present in the training set. Xiang et al. [28] investigated the fatigue property of natural rubber composites through the BPNN model and conducted sensitivity analysis to assess the varying degrees of influence of input features on the fatigue life. Considering the history-dependent phenomenon in the fatigue of materials, Jian et al. [29] established a novel Double-layer Bidirectional Long Short-Term Memory (BILSTM) neural network model, which integrates both transfer learning and attention mechanism, to predict the fatigue life of thin plate structures made of carbon fibre reinforced polymers, and the model achieved the best performance compared to the Long Short-Term Memory (LSTM) and LSTM with transfer learning models. Although machine learning methods are widely applied, they require large amounts of data for effective training and to prevent overfitting due to their purely data-driven nature [30-31]. Furthermore, such models make predictions based on a black-box mechanism with the absence of physical explanation, which may lead to physically inconsistent results [32].

PINN are advanced predictive models that incorporate physical laws with data-driven approaches [33-34]. By incorporating physical constraints as regularization terms into the loss function, PINN models have proven to be efficient in addressing key challenges in fatigue life prediction, including data scarcity and high data disparity [35-37]. Li et al. [38] reviewed the developments of physics-informed data-driven prediction methods for the Remaining Useful Life (RUL), which includes physical model and data fusion methods, stochastic degradation model based methods, and physics-informed machine learning based methods. The results showed that the physics-informed machine learning based methods achieved the best performance in several benchmark case studies, including the bridge deck rebar corrosion datasets, the Commercial Modular Aero-Propulsion System Simulation (C-MAPSS) datasets, and the lithium battery aging datasets. Liao et al. [39] proposed a path-dependent adaptive PINN model that integrated a genetic algorithm and meta-learning framework to optimize model weights. The model exhibited superior prediction performance for multiaxial fatigue life of stainless steel, with most predictions falling within the 1.5-factor error bands. Zhai et al. [40] established a coupled data/physics-driven simulation framework for accurate and efficient simulation of a three-story frame/reinforcement concrete shear-wall building. This framework leveraged the complementary strengths of both data-driven and physics-driven models and achieved a computational speed-up of more than 70 times compared to the refined Abaqus model. Dang et al. [36] studied the fatigue behaviour of laser-directed energy deposition Ti-6AI-4V using a novel prediction framework based on the PINN algorithm. The influence patterns of various fatigue-sensitive parameters were studied, showing the effectiveness and interpretability of the proposed method. Dong et al. [41] introduced a fracture mechanics-based PINN for the prediction of multi-defect materials. Owing to the incorporation of physical knowledge, a coefficient of determination exceeding 0.9 has been achieved. Hao et al. [42] developed an innovative damage physics-informed neural network for multi-mode fatigue failure assessment of Ni-based superalloys using pure-loading datasets, achieving better predictive performance than purely data-driven and physics-based models. Baktheer et al. [43] proposed a physics-based machine learning framework to predict the fatigue lifetime of high-strength concrete under non-uniform loading scenarios, offering more accurate predictions than data-driven neural network with limited training data.

Despite the various applications of PINN models in fatigue prediction scenarios, their use in grouted connections remains limited due to the complex physical mechanisms and the lack of publicly available datasets. To address this research gap, a novel hybrid PINN model, which integrates both simplified physical constraints and hidden physical laws that relate fatigue life to fatigue-related parameters, is proposed in this paper to predict the fatigue life of axially loaded grouted connections. In addition, this work conducts SHAP analysis and physical consistency analysis to interpret the developed hybrid PINN model. To support the training and evaluation of the proposed model, a fatigue dataset is constructed using the data from the open literature, subjected to several data preparation processes, including Pearson correlation coefficient analysis, stratified random splitting, and data normalization.

2. Dataset establishment of fatigue test on grouted connections

2.1. Fatigue test data of grouted connections

The configuration of the grouted connection is shown in Fig. 2, which consists of two cylindrical steel tubes of different diameters. The annular gap between the tubes is filled with a grout material. As part of the composite design, ring-shaped shear keys are installed along the opposing steel surfaces to enhance interfacial shear strength. During service, the fatigue performance of this structure is influenced by multiple factors, including structural geometry, material properties, and loading conditions. To develop an effective fatigue life prediction model for axially loaded grouted connections, a dataset comprising 70 samples is established based on the open literature [3,4,6,19,20,44,45,46]. The established dataset includes 19 input features and the target output of fatigue life. Details of each sample are listed in Table A.1 in the Appendix. The specific input features are as follows:

(1) Structural geometry: The diameter of the sleeve (D_s); the thickness of the sleeve (t_s); the diameter of the pile (D_p); the thickness of the pile (t_p); the length of the grout (L_g); the thickness of the grout (t_g); the width of the shear key (w); and the height-to-spacing ratio of the shear key (h/s).

(2) Material properties: The elastic modulus of the sleeve (E_s); the yield strength of the sleeve ($\sigma_{\mathrm{Y\_s}}$); the elastic modulus of the pile (E_p); the yield strength of the pile ($\sigma_{\mathrm{Y\_p}}$); the ultimate compressive strength of the grout (UCS_g); the Poisson's ratio of the grout (v_g); and the Poisson's ratio of the steel (v_s).

(3) Loading conditions: The minimum load (P_min); the loading frequency (f); the loading environment (env); and the ratio of the maximum load to the static interfacial shear strength ($P_\mathrm{max}/P_\mathrm{static}$).

These features are selected to represent the comprehensive key variables affecting fatigue life. Among the input features, the "Loading environment" specifies whether the grouted connection is placed above or under water, with 0 representing an above-water condition and 1 representing an underwater condition. The inclusion of this feature demonstrates the model's applicability across different operational scenarios. It should be noted that as the “loading environment” becomes more finely categorized and the dataset is further enriched, one-hot encoding may provide a more suitable and expressive representation.

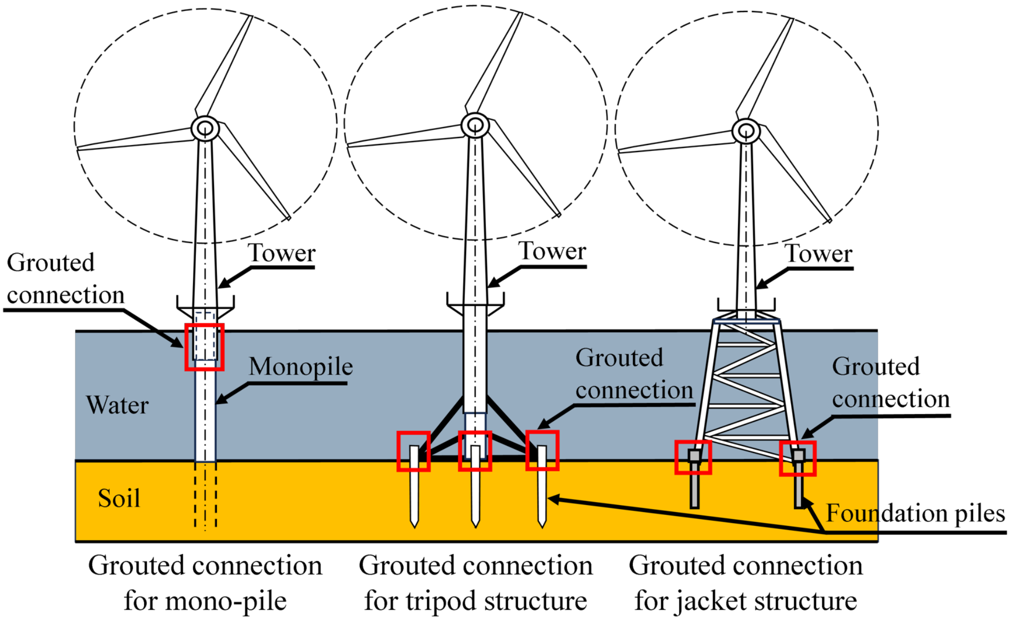

Fig. 1. Grouted connections in offshore wind turbines support structures.

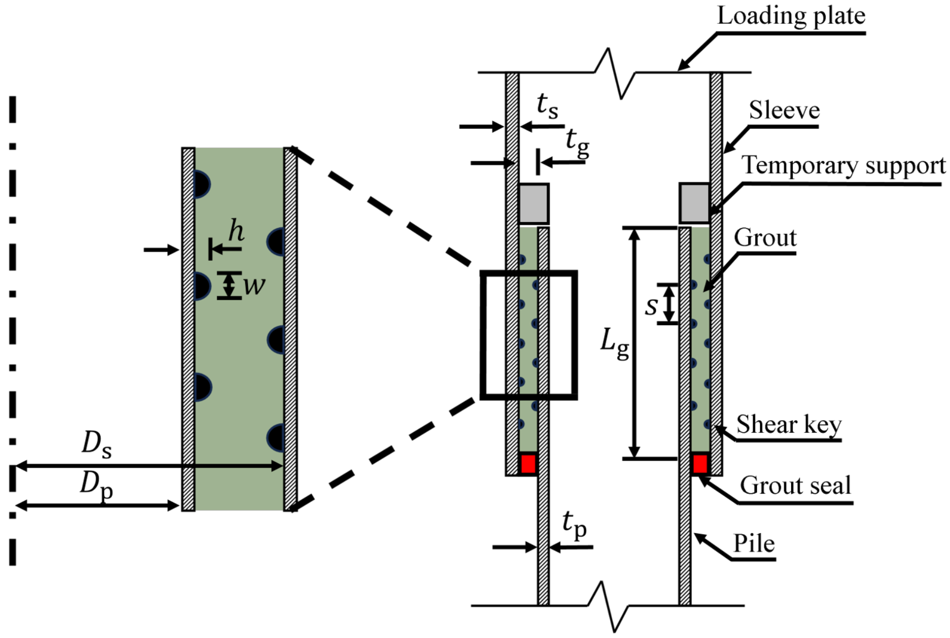

Fig. 2. Configuration of grouted connections

2.2. Dataset preprocessing

Before inputting the dataset into the neural network, the preprocessing steps are applied, including correlation analysis to avoid multicollinearity among input features and improve model accuracy; reasonable dataset partitioning to enable effective model evaluation and reduce the risk of overfitting; and normalization to accelerate training convergence.

The Pearson correlation coefficient is commonly used in statistics to measure the linear relationship between two variables, *x* and *y*, and it can be calculated by:

$$r = \frac{\operatorname{cov}(x, y)}{\sqrt{\operatorname{var}(x) \cdot \operatorname{var}(y)}} \tag{1}$$

where var(*x*) and var(*y*) are the variances of variables *x* and *y*, respectively, and cov(*x*, *y*) is their covariance. The value of *r* ranges from -1 to 1. If $|r| > 0.7$, it indicates a strong linear relationship between x and y. If $|r| < 0.2$, the relationship is considered weak, and any value in between is considered moderate. In this study, the correlations between 18 input features are calculated, since the feature, v_s, is constant throughout the dataset and thus excluded from the correlation analysis. The corresponding heatmap is shown in Fig. 3.

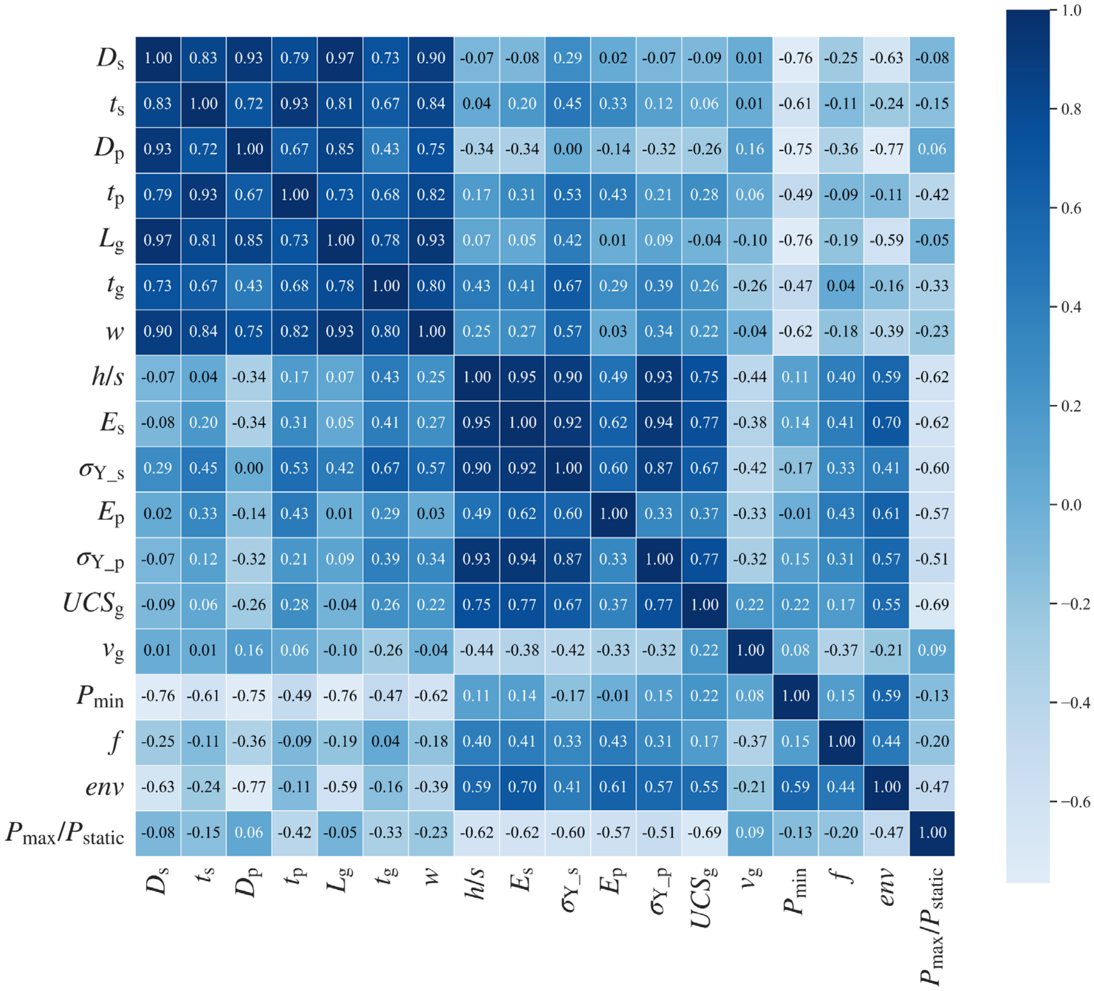

	D_s	t_s	D_p	t_p	L_g	t_g	w	h/s	E_s	σ_{Y_s}	E_p	σ_{Y_p}	UCS_g	v_g	P_{min}	f	env	P_{max}/P_{static}
D_s	1.00	0.83	0.93	0.79	0.97	0.73	0.90	-0.07	-0.08	0.29	0.02	-0.07	-0.09	0.01	-0.76	-0.25	-0.63	-0.08
t_s	0.83	1.00	0.72	0.93	0.81	0.67	0.84	0.04	0.20	0.45	0.33	0.12	0.06	0.01	-0.61	-0.11	-0.24	-0.15
D_p	0.93	0.72	1.00	0.67	0.85	0.43	0.75	-0.34	-0.34	0.00	-0.14	-0.32	-0.26	0.16	-0.75	-0.36	-0.77	0.06
t_p	0.79	0.93	0.67	1.00	0.73	0.68	0.82	0.17	0.31	0.53	0.43	0.21	0.28	0.06	-0.49	-0.09	-0.11	-0.42
L_g	0.97	0.81	0.85	0.73	1.00	0.78	0.93	0.07	0.05	0.42	0.01	0.09	-0.04	-0.10	-0.76	-0.19	-0.59	-0.05
t_g	0.73	0.67	0.43	0.68	0.78	1.00	0.80	0.43	0.41	0.67	0.29	0.39	0.26	-0.26	-0.47	0.04	-0.16	-0.33
w	0.90	0.84	0.75	0.82	0.93	0.80	1.00	0.25	0.27	0.57	0.03	0.34	0.22	-0.04	-0.62	-0.18	-0.39	-0.23
h/s	-0.07	0.04	-0.34	0.17	0.07	0.43	0.25	1.00	0.95	0.90	0.49	0.93	0.75	-0.44	0.11	0.40	0.59	-0.62
E_s	-0.08	0.20	-0.34	0.31	0.05	0.41	0.27	0.95	1.00	0.92	0.62	0.94	0.77	-0.38	0.14	0.41	0.70	-0.62
σ_{Y_s}	0.29	0.45	0.00	0.53	0.42	0.67	0.57	0.90	0.92	1.00	0.60	0.87	0.67	-0.42	-0.17	0.33	0.41	-0.60
E_p	0.02	0.33	-0.14	0.43	0.01	0.29	0.03	0.49	0.62	0.60	1.00	0.33	0.37	-0.33	-0.01	0.43	0.61	-0.57
σ_{Y_p}	-0.07	0.12	-0.32	0.21	0.09	0.39	0.34	0.93	0.94	0.87	0.33	1.00	0.77	-0.32	0.15	0.31	0.57	-0.51
UCS_g	-0.09	0.06	-0.26	0.28	-0.04	0.26	0.22	0.75	0.77	0.67	0.37	0.77	1.00	0.22	0.22	0.17	0.55	-0.69
v_g	0.01	0.01	0.16	0.06	-0.10	-0.26	-0.04	-0.44	-0.38	-0.42	-0.33	-0.32	0.22	1.00	0.08	-0.37	-0.21	0.09
P_{min}	-0.76	-0.61	-0.75	-0.49	-0.76	-0.47	-0.62	0.11	0.14	-0.17	-0.01	0.15	0.22	0.08	1.00	0.15	0.59	-0.13
f	-0.25	-0.11	-0.36	-0.09	-0.19	0.04	-0.18	0.40	0.41	0.33	0.43	0.31	0.17	-0.37	0.15	1.00	0.44	-0.20
env	-0.63	-0.24	-0.77	-0.11	-0.59	-0.16	-0.39	0.59	0.70	0.41	0.61	0.57	0.55	-0.21	0.59	0.44	1.00	-0.47
P_{max}/P_{static}	-0.08	-0.15	0.06	-0.42	-0.05	-0.33	-0.23	-0.62	-0.62	-0.60	-0.57	-0.51	-0.69	0.09	-0.13	-0.20	-0.47	1.00

Fig. 3. Heatmap of Pearson correlation coefficients for input features.

After removing the redundant input features exhibiting high correlation ($|r| > 0.7$) with the remaining features in the dataset, the number of input features is reduced to 8, which are t_{g}, h/s, E_{p}, v_{s}, P_{min}, f, env, and $P_{\mathrm{max}}/P_{\mathrm{static}}$. Since E_{p} and v_{s} remain nearly constant over the data, they are removed from the model to focus on the contribution of more informative features. Therefore, the constructed dataset comprises 6 input features and 1 output feature. It can be seen that the incorporation of the dimensionless parameters among the input features h/s and $P_{\mathrm{max}}/P_{\mathrm{static}}$ provides physically meaningful and scale-independent descriptors for the geometric and loading characteristics of grouted connections. These descriptors make the dataset representative of a broad range of configurations and thereby enhance the model's generalization capability.

The dataset is then split into a 60%-40% train-test ratio, which is used for small datasets to retain enough data for reliable evaluation. Since the fatigue life is highly dispersed and is widely varied ranging from a few to several million cycles, a stratified random splitting strategy is adopted to ensure that samples are evenly distributed across the fatigue life range space in both the training and testing sets: First, the data are sorted in ascending order of the fatigue life. Second, each 5 consecutive samples are formed into a group. 3 samples are randomly assigned to the training set and 2 to the testing set. Fig. 4 shows the distribution of the training and testing samples across fatigue life. It can be seen that both datasets are evenly spread across the range from 10^0 to 10^7. After sorting, the splitting bias can be reduced and the reliability of the predictive model can be enhanced. In addition, the training set is further divided into 5 folds using a similar stratified strategy for five-fold cross-validation and hyperparameter tuning.

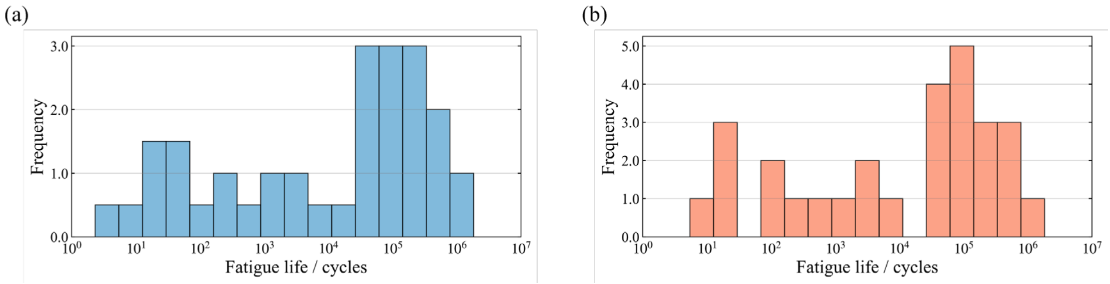

Fig. 4. Distribution of samples across fatigue life for (a) training samples and (b) testing samples.

Finally, to account for the varying scales of the input features, z-score normalization is applied to standardize the data. For the output fatigue life, a log-transformation is used to reduce the disparity, making the data more suitable for subsequent prediction.

3. Machine Learning Methodology

3.1. Development of DNN model

Artificial Neural Network (ANN), which is a biologically inspired computational network, is a robust and promising machine learning approach in extracting nonlinear hidden relationship between input and output features and has therefore found wide applications in modeling the mechanical behaviour of materials and structures [47-49]. When a neural network consists of more than 3 layers, it is considered a DNN. In this study, a back-propagation DNN regression model is constructed to predict fatigue life of axially loaded grouted connections (as shown in Fig. 5), in which the mean squared error between the logarithms of the true and predicted fatigue life (Eqs. (2)) is adopted as the loss function:

$$Loss_{\mathrm{mse}} = \frac{1}{n}\sum_{i=1}^{n}\left(\lg N_{\mathrm{true}}^{i} - \lg N_{\mathrm{pred}}^{i}\right)^{2} \tag{2}$$

where n is the number of samples in a batch, N_{true} is the true value of experimental fatigue life and N_{pred} is the predicted fatigue life.

A grid search method with five-fold cross-validation is employed in the data training process to determine the optimal network structure and parameters. As demonstrated in Fig. 5, 5 hidden layers of 128 neurons each are used to map the 6-dimensional input to a single fatigue life output. The 'Tanh' is used as the activation function and the DNN is trained using the ADAM-Optimizer with a learning rate of 0.001 for 570 epochs and a batch size of 3.

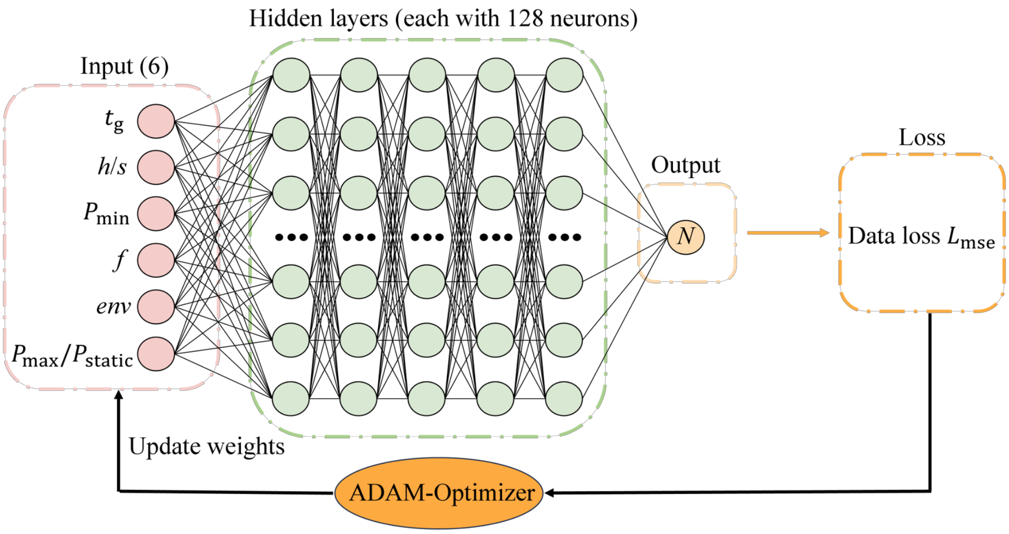

Fig. 5. Architecture of the proposed DNN model.

3.2. Development of PINN model

PINN is an innovative approach combining deep learning with physical constraints to solve partial differential equations. By penalizing the output that violates physical laws, the solution space is restricted to a manageable size and strong generalization capability can be achieved using scarce training data. Inspired by the observed correlation between the load level and fatigue life (as shown in Fig. 6), where the load level is represented by $P_{\max}/P_{\text{static}}$ in the input features and the fatigue life by N in the output, this work develops two distinct types of PINN models that incorporate either simplified physical constraints (S-PINN) or hidden physical laws (H-PINN) as regularization terms in the loss function. Furthermore, a hybrid PINN model integrating both types of physical constraints is also investigated.

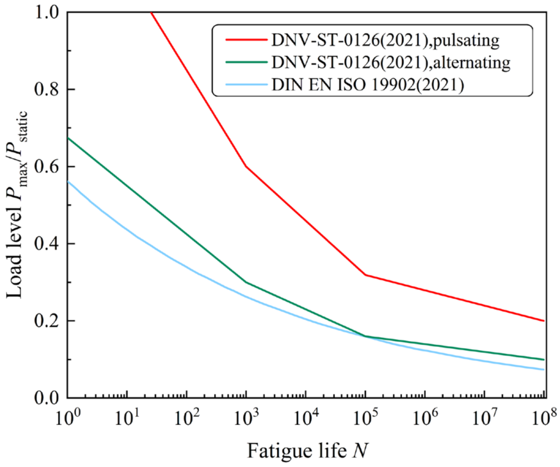

Fig. 6. S-N curves of DNV-ST-0126 [17] and DIN EN ISO 19902[18].

From Fig. 6, it's evident that the fatigue life decreases with increasing load level, and the decrease becomes more rapid at higher load levels. This trend indicates that the first-order derivative of fatigue life with respect to load level is negative, and the second-order derivative is positive, which can be expressed as:

$$\frac{\partial N}{\partial\left(P_{\max}/P_{\text{static}}\right)} \leq 0 \tag{3}$$

$$\frac{\partial^2 N}{\partial^2\left(P_{\max}/P_{\text{static}}\right)} \geq 0 \tag{4}$$

It should be noted that the fatigue life is log-transformed, and the load level is standardized using z-score normalization during data preprocessing. Accordingly, the corresponding terms in Eqs. (3)-(4) should be adjusted, and the loss function of the PINN model incorporating simplified physical constraints can be written as:

$$Loss_{\mathrm{total}} = Loss_{\mathrm{mse}} + \omega Loss_{\mathrm{physical}} \tag{5}$$

$$\begin{gathered} Loss_{\mathrm{physical}} = \frac{1}{n}\sum_{i=1}^{n}\max\left(0, \frac{\partial \lg N_{\mathrm{pred}}^{i}}{\partial\left(\mathrm{z}\left(P_{\max}/P_{\mathrm{static}}\right)\right)^{i}}\right) + \\ \max\left(0, -\frac{\partial^{2} \lg N_{\mathrm{pred}}^{i}}{\partial^{2}\left(\mathrm{z}\left(P_{\max}/P_{\mathrm{static}}\right)\right)^{i}}\right) \end{gathered} \tag{6}$$

where $\mathrm{z}(P_{max}/P_{static})$ represents the z-score normalization of the load level. ω is the weight coefficient of physical loss. When $\omega = 0$, the PINN degenerates into the corresponding data-driven DNN model. The max operator is employed to penalize predictions deviated from the physical constraints, with the penalty increasing as the deviation distance increases.

The integration of hidden physical laws into the neural network is based on the Basquin relation, which describes the correlation between load level and fatigue life (as shown in Fig. 6), and can be expressed as:

$$\lg\left(P_{\max}/P_{\mathrm{static}}\right) = A + B\lg N \tag{7}$$

where A and B are implicit constants that depend on the structural geometry, material properties and loading conditions of the grouted connections. In this study, an additional DNN model is employed to regress A and B based on the 6-dimensional input features of each type of grouted connection. The regressed A and B are incorporated into the Basquin equation, forming the hidden physical constraint embedded in the loss function of the PINN model, which is defined as:

$$Loss_{\text{total}} = Loss_{\text{mse}} + \gamma Loss_{\text{hidden physical}} \tag{8}$$

$$Loss_{\text{hidden physical}} = \frac{1}{n}\sum_{i=1}^{n}\left(\lg\left(P_{\max}/P_{\text{static}}\right)^{i} - A^{i} - B^{i}\lg N_{\text{pred}}^{i}\right) \tag{9}$$

where γ is the weight coefficient of hidden physical loss. As γ increases, the model is increasingly penalized for violating the underlying physical law.

Figs. (7)-(9) illustrate the constructed S-PINN, H-PINN and hybrid PINN models, respectively. The loss functions of the S-PINN and H-PINN models are derived from Eqs. (5), (6), (8) and (9), whereas the loss function of the hybrid PINN model is expressed as:

$$Loss_{\text{total}} = Loss_{\text{mse}} + \omega Loss_{\text{physical}} + \gamma Loss_{\text{hidden physical}} \tag{10}$$

where ω is the weight coefficient of physical loss, and γ is that of the hidden physical loss.

In this work, the main structures of the three types of PINN models based on different physical constraints remain consistent with the DNN model. In the training of PINN models, data loss and physical loss converge at different rates. Inappropriate weight setting may lead to a bias towards a certain loss function or cause training instability. To select the benchmark weights for the physical loss and hidden physical loss, their magnitudes are compared with that of the data loss. The weights are then set to ensure that all losses are of comparable scale. For example, if the data loss is around 1, while the other loss is around 0.1, a weight coefficient of 10 is assigned to balance their contributions. Based on this, a further grid search with five-fold cross-validation is performed to fine-tune the benchmark weights and identify the optimal values. In this paper, the weight coefficients are set to 0.5 for the physical loss and 0.1 for the hidden physical loss across the three PINN models. The DNN used to regress the parameters, *A* and *B,* in the Basquin relation consists of 3 hidden layers of 128 neurons each, and ‘Tanh’ is used as the activation function. For more complex models, more advanced hyperparameter optimization strategies, such as random search, Bayesian optimization, and evolutionary or population-based optimization algorithms, may offer greater potential to reduce computational costs and accelerate model convergence.

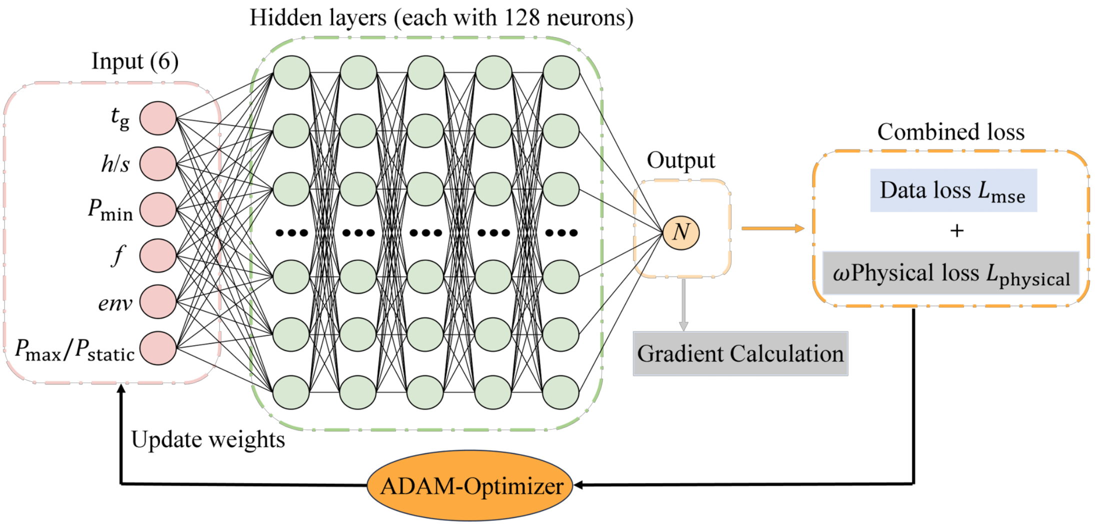

Fig. 7. Architecture of the proposed S-PINN model.

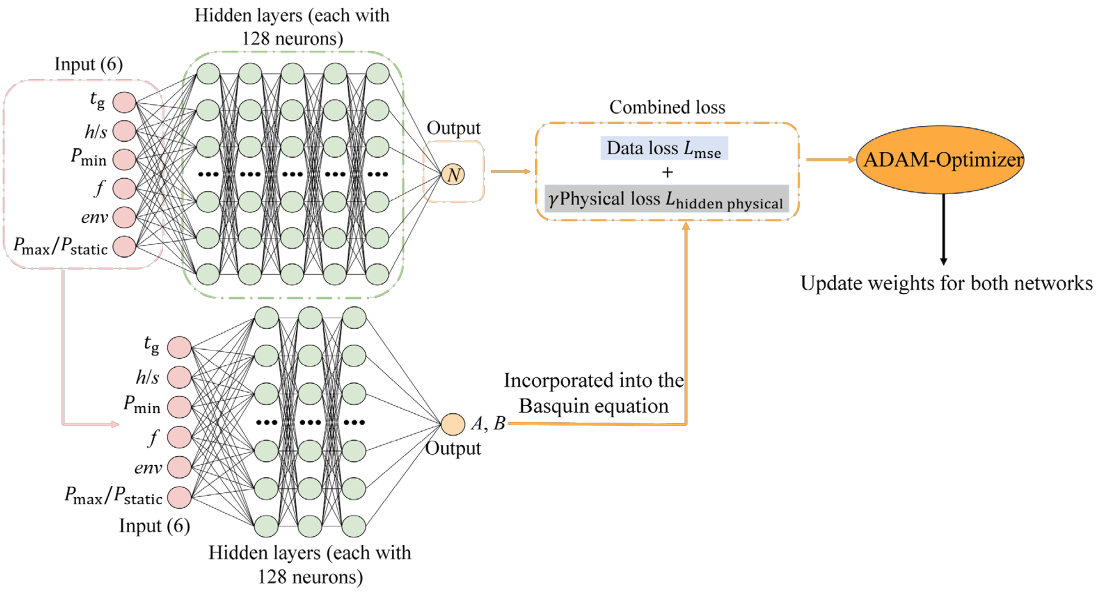

Fig. 8. Architecture of the proposed H-PINN model.

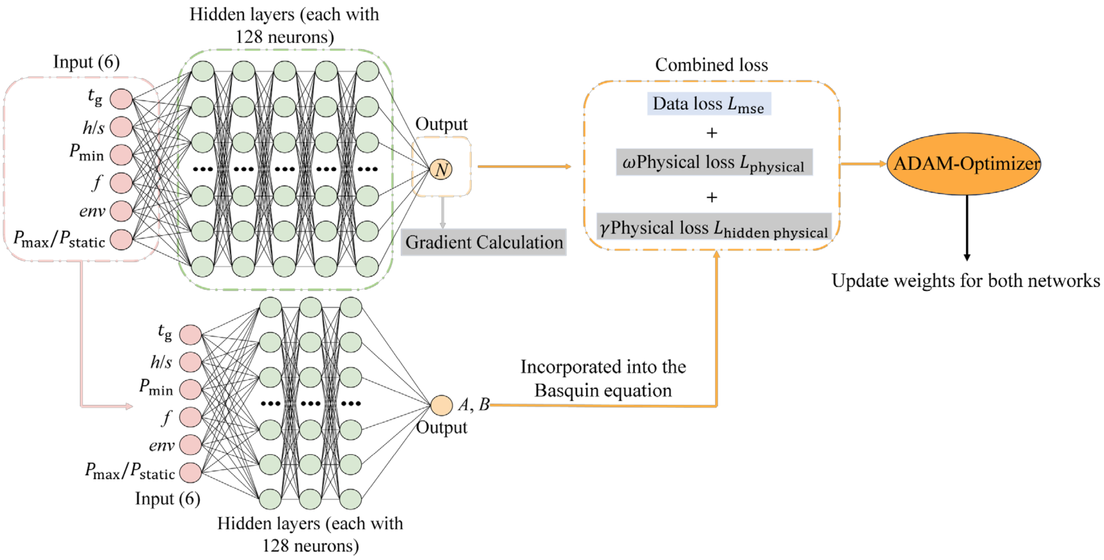

Fig. 9. Architecture of the proposed hybrid PINN model.

3.3. Model interpretation and evaluation

The SHAP method is widely applied to interpret machine learning models. In addition to identifying the importance of each feature in the model's prediction, SHAP analysis enables a more profound exploration of the positive or negative contribution of each feature [50]. In this work, the GradientSHAP algorithm is implemented to interpret the developed hybrid PINN model, and the importance and contribution of each feature to the prediction of fatigue life are investigated.

The Mean Square Error (*MSE*) and the Coefficient of Determination (R^2) are used as the evaluation metrics to assess the accuracy of the model's prediction, which are defined as:

$$MSE = \frac{1}{n}\sum_{i=1}^{n}\left(\lg N_{\text{true}}^{i} - \lg N_{\text{pred}}^{i}\right)^{2} \tag{11}$$

$$R^{2} = 1 - \frac{\sum_{i=1}^{n}\left(\lg N_{\text{true}}^{i} - \lg N_{\text{pred}}^{i}\right)^{2}}{\sum_{i=1}^{n}\left(\lg N_{\text{true}}^{i} - \lg N_{\text{average}}\right)^{2}} \tag{12}$$

where $\lg N_{\text{average}}$ is the average of $\lg N_{\text{true}}$. In evaluating model performance, a larger *MSE* indicates that the data are widely dispersed around the mean, while a smaller R^2 indicates a poor fitting ability of the model.

4. Fatigue life predictions and discussion

4.1. Prediction results using different machine learning models

In this work, the input features to the machine learning models for the grouted connections are reduced to 8 through Pearson correlation coefficient analysis by eliminating redundant features that exhibit high correlation with others in the dataset, which helps reduce multicollinearity while remaining consistent with prior physical knowledge. In this process, the t_{g} and h/s, which govern the load transfer path and local shear failure mechanism, are retained as stress concentration regions are more influential in determining fatigue behaviour than global geometric dimensions. The E_{s}, E_{p}, v_{g}, and

v_{s} are removed due to their limited variation within the dataset, as they are associated with standardized materials commonly used in engineering practice. For the removal of $\sigma_{\mathrm{Y\_s}}$, $\sigma_{\mathrm{Y\_p}}$, and UCS_{g}, the yield strengths primarily affect the ultimate load-bearing capacity of grouted connections, rather than contributing continuously to fatigue performance [51]. The UCS_{g} shows a similar correlation with fatigue life compared to the h/s, with Pearson correlation coefficients of 0.55 and 0.57, respectively. Therefore, the UCS_{g} is excluded to avoid redundancy.

The network hyperparameters are critical for the convergence and reliability of predictive models. Considering the limited fatigue dataset for axially loaded grouted connections, the five-fold cross-validation process could exhibit instability, consequently compromising the reliability of the model training. To demonstrate the effectiveness of the selected hyperparameters, the prediction performance of the DNN model with different hidden layer neuron numbers is presented in Table 1, while the prediction performance of the hybrid PINN model under various combinations of the weight coefficients ω and γ is shown in Table 2. From the results, the models with the chosen hyperparameters perform the best. In contrast, the DNN model with a hidden layer neuron configuration of (64,128,256,128,64) yields the poorest performance, with an *MSE* of 0.6463 and an R^2 of 0.7350. For the hybrid PINN model, the combination of $\omega = 0.5$ and $\gamma = 0.3$ leads to the lowest accuracy, resulting in an *MSE* of 0.7197 and an R^2 of 0.7048. These results further validate the robustness of the selected hyperparameter settings.

Table 1: Prediction performance of the DNN model under different numbers of hidden layer neurons.

Hidden layer neurons	MSE	R^2
(64,64,64,64,64)	0.5250	0.7847
(128,128,128,128,128)	0.5013	0.7944
(256,256,256,256,256)	0.5837	0.7606
(64,128,256,128,64)	0.6463	0.7350
(256,256,128,128,64)	0.5275	0.7837
(128,128,64,64,32)	0.6093	0.7501

Table 2: Prediction performance of the hybrid PINN model under different combinations of the weight coefficients.

Value of ω	Value of γ	MSE	R^2
Fixed at 0.5	0.05	0.2746	0.8874
	0.1	0.2248	0.9078
	0.15	0.3272	0.8658
	0.2	0.4508	0.8151
	0.25	0.5847	0.7602
	0.3	0.7197	0.7048
0.35	Fixed at 0.1	0.2920	0.8802
0.4		0.3424	0.8596
0.45		0.3638	0.8508

0.55	0.2900	0.8811
0.6	0.3520	0.8556
0.65	0.2957	0.8787

Fig. 10 shows the fatigue life prediction results for axially loaded grouted connections using the design codes DNV-ST-0126, DIN EN ISO 19902, and the proposed DNN, S-PINN, H-PINN, and hybrid PINN models. As shown in the results, the methodologies adopted in both design codes are inadequate, with only a limited number of predictions falling within the 3-factor error bands. Moreover, the applicability of the DIN EN ISO 19902 code is restricted when dealing with structures subjected to pulsating compression loads, highlighting the necessity of developing new models, including machine learning-based models for more accurate fatigue life prediction. Among the proposed models, the hybrid PINN model, which incorporates both simplified physical constraints and hidden physical laws as the regularization terms, demonstrates the best prediction performance. Most of its predictions fall within the 3-factor error bands, except for 3 outliers corresponding to the structures with low fatigue life. It can be seen that the predictions of the three structures from other models fall also outside the 3-factor error bands, which can be attributed to the scarcity of training data in the low-fatigue-life range. While the hybrid PINN has reduced deviation, more training data in this range are required to improve the model.

In comparison, the predicted fatigue life of the S-PINN model has 5 points outside the 3-factor error bands, showing better accuracy than the purely data-driven DNN model, which has 7 such predictions. In contrast, the H-PINN model exhibits the greatest dispersion, with 11 predictions falling outside the bands. These results indicate that incorporating the first- and second-order derivatives of fatigue life with respect to load level guides the model to converge in a more physically consistent direction. However, the lack of explicit physical formulation limits the potential to further improve accuracy. The poor predictive performance of the H-PINN model demonstrates that when explicit physical equations contain implicit parameters, such as the constants *A* and *B* in the Basquin relation which vary for different grouted connections, the use of such equations as model constraints should be complemented with additional prior physical knowledge to enhance model reliability.

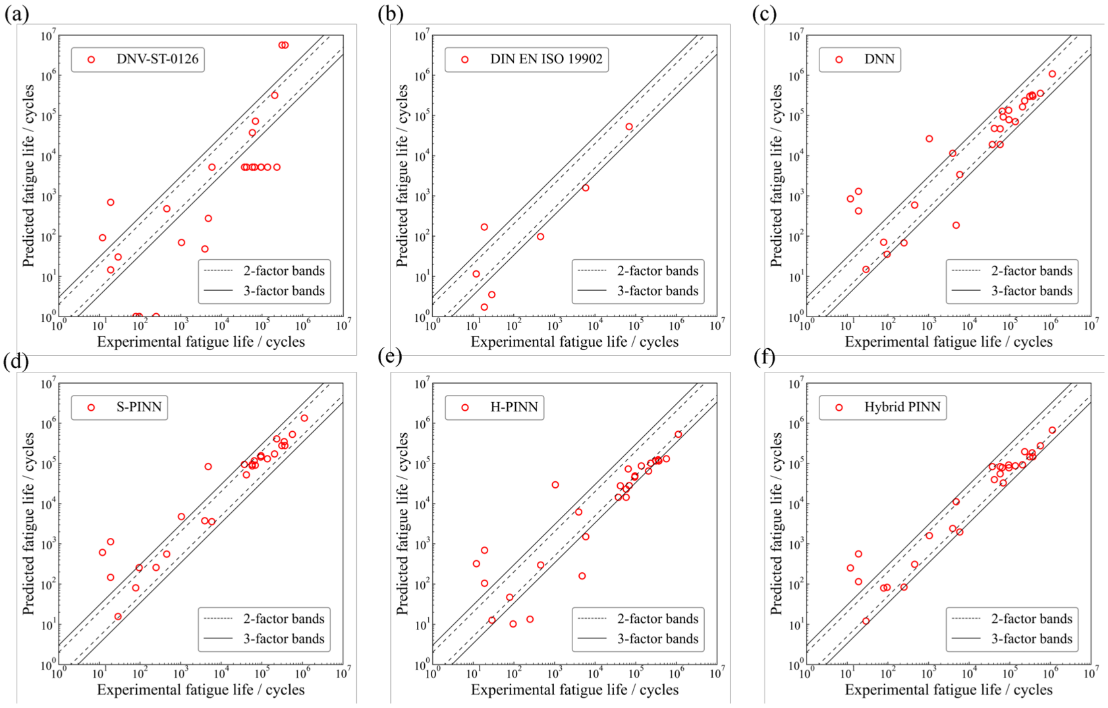

Fig. 10. Fatigue life prediction results of axially loaded grouted connections by (a) DNV-ST-0126; (b) DIN EN ISO 19902; (c) DNN; (d) S-PINN; (e) H-PINN; (f)

Hybrid PINN.

Furthermore, the prediction performance of the proposed models is assessed by utilizing the evaluation parameters *MSE* and R^2, which are calculated according to Eqs. (11)-(12) and is illustrated in Fig. 11. It can be evaluated that the hybrid PINN model achieves the lowest *MSE* of 0.2248 and the highest R^2 of 0.9078, indicating that the integration of simplified physical constraints and hidden physical laws significantly enhances the model's generalization capability. In contrast, the H-PINN model has the highest *MSE* of 0.5413 and the lowest R^2 of 0.7780, which performs worse than the conventional DNN model. This further demonstrates that the effectiveness of a PINN model depends heavily on the accuracy of the physical constraints, and inaccurate prior physical knowledge may mislead the training process and limit the model's representational capacity.

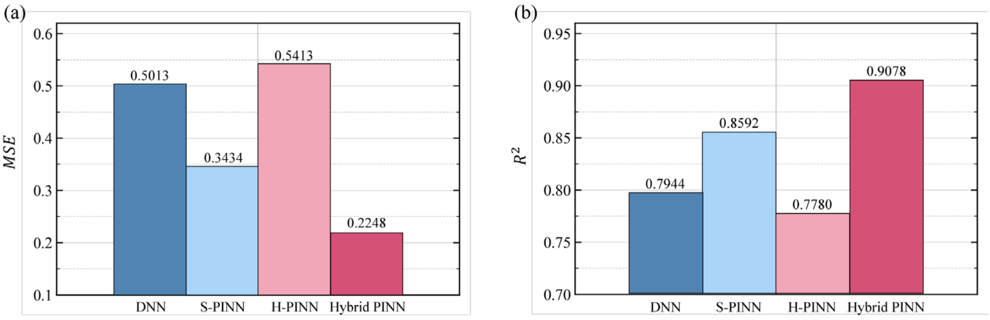

Fig. 11. Prediction performance of different models: (a) *MSE*; (b) R^2.

Fig. 12 depicts the evolution of the loss functions among the proposed models during training. It can be observed that the total loss for the H-PINN and hybrid PINN models is higher than that of the DNN and S-PINN models, which are caused by the inclusion of the Basquin relation as the hidden physical law in the loss function. Meanwhile, the DNN model exhibits the most fluctuations at around 320 epochs. This behaviour mainly results from the increased sensitivity to noise and unstable optimization process due to the absence of physical guidance. In contrast, the incorporation of simplified physical constraints in the S-PINN model helps suppress such fluctuations. However, the use of soft inequality constraints can lead to gradient discontinuities and a weakened gradient signal, especially near the constraint boundaries, which results in the localized instabilities at around 350 and 510 epochs. Compared to the DNN and S-PINN models, the H-PINN and hybrid PINN models exhibit more stable training behaviour, demonstrating the effectiveness of incorporating the hidden physical law. The hybrid PINN model, which simultaneously incorporates simplified physical constraints and hidden physical laws as the regularization terms, achieves further improvements in prediction accuracy.

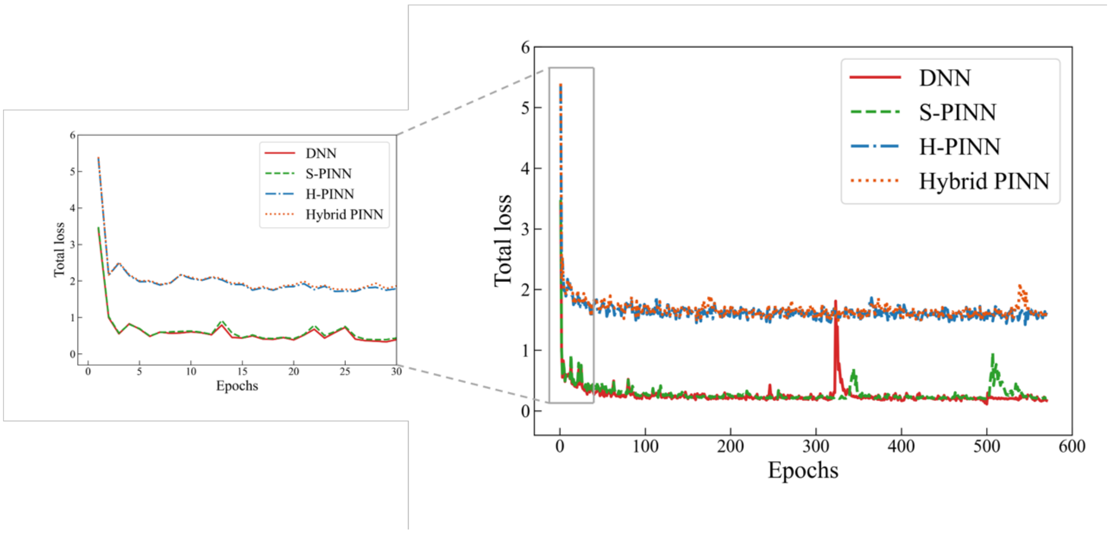

Fig. 12. The evolution of the loss functions among different prediction models.

To comprehensively understand the convergence and optimization behaviour of the hybrid PINN model, the evolution of its loss components is presented in Fig. 13. At the beginning of training, the data loss decreases rapidly and subsequently stabilizes. The occurrence of oscillations arises from the need to balance the data-driven loss with the physics-based constraints during optimization. The physical loss quickly approaches zero, indicating that the corresponding soft inequality constraints is easy to satisfy. In contrast, the hidden physical loss remains within a stable range, and the regularization effect introduced by the hidden physical constraint helps prevent the data loss from overfitting to the limited training samples, thereby enhancing the generalization capability of the hybrid PINN model.

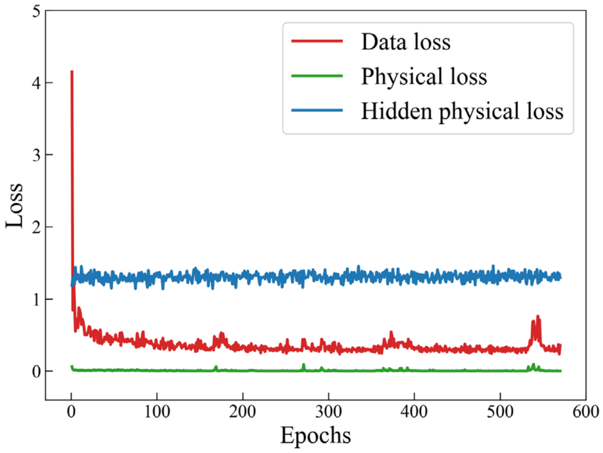

Fig. 13. The evolution of the loss components in the hybrid PINN model.

4.2. Interpretive analysis of the hybrid PINN model

The hybrid PINN model demonstrates excellent performance in predicting fatigue life of axially loaded grouted connections. To study further the predictions of the model, interpretive analysis is conducted on the test data using SHAP analysis and physical consistency evaluation. Fig. 14 presents the SHAP summary plot illustrating the contributions of the selected features to the predicted fatigue life. In this plot, the SHAP value represents the quantitative contribution of each feature to the model output, with positive SHAP values indicating an increase in the predicted fatigue life, whereas negative values indicate a decrease. The colour of the points reflects the feature values, with blue corresponding to lower values and red to higher values. The features are ranked from top to bottom according to their average absolute SHAP value, which represents their overall importance in the model's predictions. It can be observed that f and t_g contribute the least to the model's predictions, with their SHAP values largely centered around 0. However, higher values of these features could still have a directional influence on the predictions. This may be attributed to the limited variation of these two features within the dataset, which reduces their informational value and weakens their influence on the decision-making process of the model. Their influence on the model's output is localized and occurs only when their values deviate substantially from the mean.

The contributions of the remaining features are analyzed and found to be consistent with known fatigue mechanisms in grouted connections. For h/s, larger height-to-spacing ratio of the shear key enhances mechanical interlocking, reduces interface slip, and delays crack initiation at the shear-key tips. These effects slow down the accumulation of fatigue damage, resulting in improved fatigue resistance. For the loading parameters, a higher P_min reduces loading fluctuation and slows fatigue crack propagation, whereas a higher $P_\mathrm{max}/P_\mathrm{static}$ indicates a larger cyclic loading range, which accelerates fatigue failure processes in grouted connections, such as grout cracking, grout crush, and interface slip, thereby leading to opposite influences on the fatigue behaviour. For *env*, a feature value of 1 represents that the grouted connections are deployed underwater. In such conditions, cyclic hydraulic pressure can cause grout erosion, promote early cracking, and increase the relative slip at the interface, which together accelerate fatigue degradation and reduce the fatigue life.

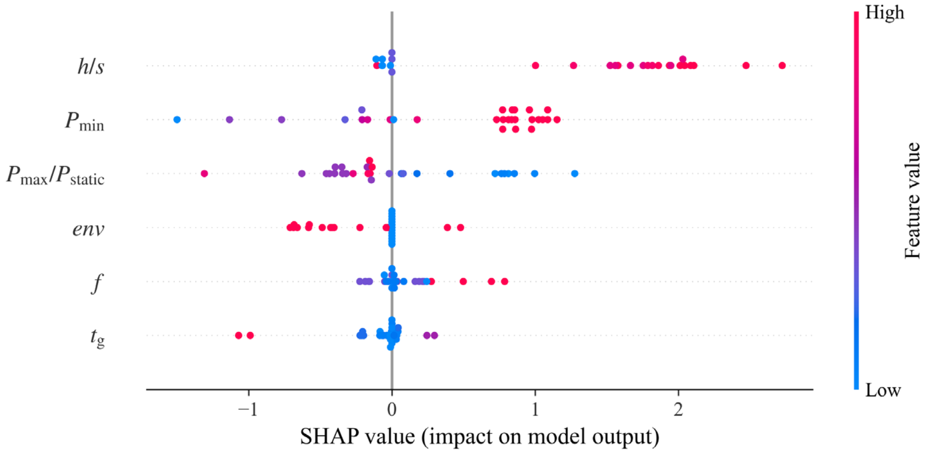

Fig. 14. Results of SHAP analysis for the hybrid PINN model.

Fig. 15 shows the predicted first- and second-order derivatives of fatigue life with respect to load level for both the DNN and hybrid PINN models. It is evident that due to the incorporation of the physical constraints, the hybrid PINN model tends to produce physically consistent predictions on the unseen data, which in turn enhances the reliability of the model. In contrast, even though the purely data-driven DNN model is capable of achieving acceptable prediction accuracy, it produces extreme outliers that significantly violate physical constraints described in Eqs. (3)-(4), which undermines the physical robustness of the model and limits its generalization capability in unseen scenarios.

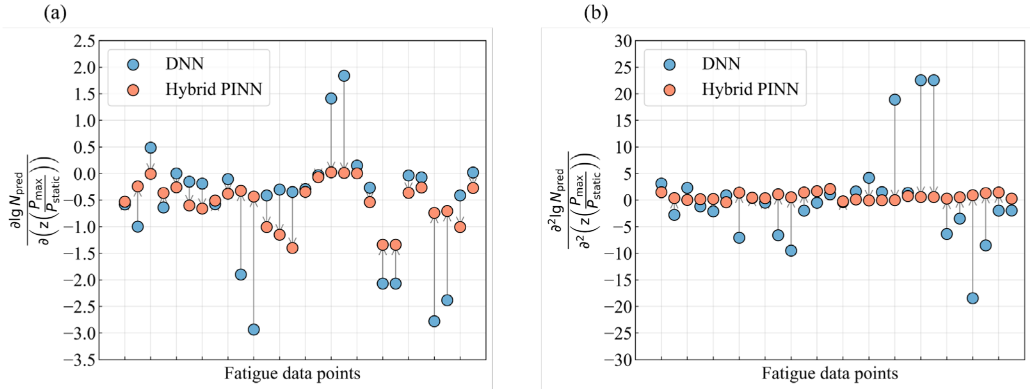

Fig. 15. Physical consistency analysis of proposed DNN and hybrid PINN models: (a) First-order derivative trend and (b) Second-order derivative trend of fatigue life with respect to load level.

5. Conclusions

A novel hybrid PINN model is developed to predict the fatigue life of axially loaded grouted connections. The model integrates both simplified physical constraints and hidden physical laws, and is based on a dataset constructed from the open literature. To further understand the mechanisms of the model, SHAP analysis and physical consistency analysis are conducted for model interpretation. Based on the prediction results, the following conclusions are made:

(1) Although the DNN model can achieve acceptable prediction accuracy in estimating fatigue life of axially loaded grouted connections, it may produce predictions that severely violate physical laws. The results demonstrate that the predictive performance of purely data-driven models heavily depends on the distribution alignment between the training and the testing datasets.

(2) A novel hybrid PINN model incorporating both simplified physical constraints and hidden physical laws is developed to predict the fatigue life of axially loaded grouted connections. Guiding the learning process in a manner consistent with physical principles, the hybrid PINN model achieves the best fatigue life prediction performance among the DNN, S-PINN, and H-PINN models, with the lowest MSE of 0.2248 and the highest R^2 of 0.9078.

(3) The SHAP analysis identifies the height-to-spacing ratio of the shear key (h/s) and the minimum load ($P_{\min}$) as the two most influential features affecting the fatigue behaviour of axially loaded grouted connections, Furthermore, the physical consistency analysis confirms that the hybrid PINN model can generate physically consistent predictions on unseen data, demonstrating the model's reliability and generalization capability.

Based on the findings of this paper, the proposed model can be extended to a dynamic prediction framework. As more data become available, the model can be updated through a warm-start fine-tuning strategy, in which the previously trained network serves as the initialization while the original architecture and physics-based loss components are retained. Furthermore, further investigations could explore more accurate and detailed fatigue prediction by incorporating different forms of physical constraints, as well as different failure modes of grouted connections, such as crack failure of grout and steel, into the model. In addition, conducting additional representative fatigue experiments will be essential to further verify the extrapolation capability of the proposed model under previously unseen conditions.

The current work is limited to fatigue prediction based on macroscopic features. Developing a cross-scale fatigue life prediction framework that integrates microscale damage evolution, mesoscale interfacial response, and macroscale fatigue behaviour is possible under the framework established in this paper and represents an important direction for future research.

Date availability

Data will be made available on request.

Acknowledgments

The authors would like to acknowledge the research grant received from the Guangdong Outstanding Youth Fund (Grants No. 2022B1515020037), Shenzhen Fundamental Research Project (Grant No. JCYJ20240813143019025), and Shenzhen High-level Talent Team Project (No. KQTD20200820113004005).

Appendix

See Table A.1.

Table A.1: Fatigue test database for grouted connections

Source	Year	D_s (mm)	t_s (mm)	D_p (mm)	t_p (mm)	L_g (mm)	t_g (mm)	w (mm)	h/s	E_s (GPa)	$\sigma_{\mathrm{Y\_s}}$ (MPa)	E_p (GPa)	$\sigma_{\mathrm{Y\_p}}$ (MPa)	UCS_g (MPa)	v_g	v_s	P_min (kN)	f	env	$P_\mathrm{max}/P_\mathrm{static}$	N
Bechtel [3]	2016	813.0	20.0	406.4	25.00	2140.0	183.50	12.0	0.0600	210	423.0	210	360.0	140.0	0.20	0.30	-1000.00	2.00	0	0.25	5890
Bechtel [3]	2016	813.0	20.0	406.4	25.00	2140.0	183.50	12.0	0.0600	210	423.0	210	360.0	140.0	0.20	0.30	-2000.00	2.00	0	0.49	29
Bechtel [3]	2016	813.0	20.0	610.0	25.00	2140.0	81.50	12.0	0.0600	210	423.0	210	360.0	140.0	0.20	0.30	-1000.00	2.00	0	0.16	89100
Bechtel [3]	2016	813.0	20.0	610.0	25.00	2140.0	81.50	12.0	0.0600	210	423.0	210	360.0	140.0	0.20	0.30	-2000.00	2.00	0	0.33	602
Bechtel [3]	2016	813.0	20.0	610.0	25.00	2140.0	81.50	12.0	0.0600	210	423.0	210	360.0	140.0	0.20	0.30	-3000.00	2.00	0	0.49	30
Bechtel [3]	2016	813.0	20.0	406.4	25.00	2140.0	183.50	12.0	0.0600	210	423.0	210	360.0	90.0	0.18	0.30	-1000.00	2.00	0	0.27	3090
Bechtel [3]	2016	813.0	20.0	406.4	25.00	2140.0	183.50	12.0	0.0600	210	423.0	210	360.0	90.0	0.18	0.30	-2000.00	2.00	0	0.53	14
Bechtel [3]	2016	813.0	20.0	610.0	25.00	2140.0	81.50	12.0	0.0600	210	423.0	210	360.0	90.0	0.18	0.30	-1000.00	2.00	0	0.17	69183
Bechtel [3]	2016	813.0	20.0	610.0	25.00	2140.0	81.50	12.0	0.0600	210	423.0	210	360.0	90.0	0.18	0.30	-2000.00	2.00	0	0.34	457
Bechtel [3]	2016	813.0	20.0	610.0	25.00	2140.0	81.50	12.0	0.0600	210	423.0	210	360.0	90.0	0.18	0.30	-3000.00	2.00	0	0.51	20
Bechtel [3]	2016	813.0	20.0	406.4	25.00	2140.0	183.50	12.0	0.0600	210	423.0	210	360.0	90.0	0.18	0.30	-1000.00	2.00	1	0.25	95000
Raba [4]	2018	114.3	7.2	60.0	9.50	90.0	22.50	2.5	0.0625	210	355.0	210	355.0	90.0	0.18	0.30	0.00	10.00	1	0.50	36686
Raba [4]	2018	114.3	7.2	60.0	9.50	90.0	22.50	2.5	0.0625	210	355.0	210	355.0	90.0	0.18	0.30	0.00	5.00	1	0.50	58011
Raba [4]	2018	114.3	7.2	60.0	9.50	90.0	22.50	2.5	0.0625	210	355.0	210	355.0	90.0	0.18	0.30	0.00	2.00	1	0.50	137243
Raba [4]	2018	114.3	7.2	60.0	9.50	90.0	22.50	2.5	0.0625	210	355.0	210	355.0	90.0	0.18	0.30	0.00	1.00	1	0.50	87178
Raba [4]	2018	114.3	7.2	60.0	9.50	90.0	22.50	2.5	0.0625	210	355.0	210	355.0	90.0	0.18	0.30	0.00	0.30	1	0.50	233262
Raba [4]	2018	114.3	7.2	60.0	9.50	90.0	22.50	2.5	0.0625	210	355.0	210	355.0	90.0	0.18	0.30	0.00	5.00	1	0.20	1113506

Table A.1: (continued)

Source	Year	D_s (mm)	t_s (mm)	D_p (mm)	t_p (mm)	L_g (mm)	t_g (mm)	w (mm)	h/s	E_s (GPa)	σ_{Y_s} (MPa)	E_p (GPa)	σ_{Y_p} (MPa)	UCS_g (MPa)	v_g	v_s	P_{min} (kN)	f	env	P_{max}/P_{static}	N
Baba [4]	2018	114.3	7.2	60.0	9.50	90.0	22.50	2.5	0.0625	210	355.0	210	355.0	140.0	0.20	0.30	0.00	5.00	1	0.50	37279
Raba [4]	2018	114.3	7.2	60.0	9.50	90.0	22.50	2.5	0.0625	210	355.0	210	355.0	140.0	0.20	0.30	0.00	1.00	1	0.50	95624
Raba [4]	2018	114.3	7.2	60.0	9.50	90.0	22.50	2.5	0.0625	210	355.0	210	355.0	140.0	0.20	0.30	0.00	5.00	1	0.20	1118255
Raba [4]	2018	114.3	7.2	60.0	9.50	90.0	22.50	2.5	0.0625	210	355.0	210	355.0	140.0	0.20	0.30	0.00	1.00	1	0.20	1325875
Raba [4]	2018	177.8	7.2	60.0	9.50	90.0	54.25	2.5	0.0625	210	355.0	210	355.0	90.0	0.18	0.30	0.00	5.00	1	0.50	23068
Raba [4]	2018	177.8	7.2	60.0	9.50	90.0	54.25	2.5	0.0625	210	355.0	210	355.0	140.0	0.20	0.30	0.00	5.00	1	0.50	5180
Boswell et al. [6]	1986	366.0	5.0	324.0	10.00	325.0	16.00	3.0	0.0240	200	240.0	200	240.0	84.7	0.20	0.30	-400.00	0.75	0	0.43	12
Boswell et al. [6]	1986	366.0	5.0	324.0	10.00	325.0	16.00	3.0	0.0240	200	240.0	200	240.0	87.1	0.20	0.30	-300.00	0.75	0	0.32	19
Boswell et al. [6]	1986	366.0	5.0	324.0	10.00	325.0	16.00	3.0	0.0240	200	240.0	200	240.0	87.7	0.20	0.30	-500.00	0.75	0	0.53	19
Boswell et al. [6]	1986	366.0	5.0	324.0	10.00	325.0	16.00	3.0	0.0240	200	240.0	200	240.0	94.5	0.20	0.30	-275.00	0.75	0	0.28	1035
Boswell et al. [6]	1986	366.0	5.0	324.0	10.00	325.0	16.00	3.0	0.0240	200	240.0	200	240.0	93.6	0.20	0.30	-250.00	0.75	0	0.25	4205
Boswell et al. [6]	1986	366.0	5.0	324.0	10.00	325.0	16.00	3.0	0.0240	200	240.0	200	240.0	75.5	0.20	0.30	-302.00	0.75	0	0.35	1026
Lee et al. [19]	2021	267.4	6.0	190.7	6.00	760.0	32.35	8.0	0.0667	207	322.4	179	410.0	125.0	0.20	0.30	0.00	0.12	0	0.74	4800
Lee et al. [19]	2021	267.4	6.0	190.7	6.00	760.0	32.35	8.0	0.0500	207	322.4	179	410.0	125.0	0.20	0.30	0.00	0.12	0	0.58	56300
Lee et al. [19]	2021	267.4	6.0	190.7	6.00	760.0	32.35	8.0	0.0500	207	322.4	179	410.0	125.0	0.20	0.30	0.00	0.12	0	0.83	175
Borgelt et al. [20]	2024	320.0	14.0	219.0	20.00	402.5	39.00	6.0	0.0500	210	355.0	210	355.0	138.9	0.20	0.30	0.00	2.00	1	0.25	228509
Borgelt et al. [20]	2024	320.0	14.0	219.0	20.00	402.5	39.00	6.0	0.0500	210	355.0	210	355.0	138.7	0.20	0.30	0.00	2.00	1	0.22	238088
Borgelt et al. [20]	2024	320.0	14.0	219.0	20.00	402.5	39.00	6.0	0.0500	210	355.0	210	355.0	142.4	0.20	0.30	0.00	2.00	1	0.19	681270
Borgelt et al. [20]	2024	320.0	14.0	219.0	20.00	402.5	39.00	6.0	0.0500	210	355.0	210	355.0	143.3	0.20	0.30	0.00	2.00	1	0.20	232550
Borgelt et al. [20]	2024	320.0	14.0	219.0	20.00	402.5	39.00	6.0	0.0500	210	355.0	210	355.0	119.3	0.20	0.30	0.00	2.00	1	0.23	489390
Borgelt et al. [20]	2024	320.0	14.0	219.0	20.00	402.5	39.00	6.0	0.0500	210	355.0	210	355.0	128.3	0.20	0.30	0.00	2.00	1	0.20	567442

Table A.1: (continued)

Source	Year	D_s (mm)	t_s (mm)	D_p (mm)	t_p (mm)	L_g (mm)	t_g (mm)	w (mm)	h/s	E_s (GPa)	$\sigma_{\mathrm{Y\_s}}$ (MPa)	E_p (GPa)	$\sigma_{\mathrm{Y\_p}}$ (MPa)	UCS_g (MPa)	v_g	v_s	P_min (kN)	f	env	$P_\mathrm{max}/P_\mathrm{static}$	N
Borgelt et al. [20]	2024	320.0	14.0	219.0	20.00	402.5	39.00	6.0	0.0500	210	355.0	210	355.0	134.7	0.20	0.30	0.00	2.00	1	0.27	295740
Borgelt et al. [20]	2024	320.0	14.0	219.0	20.00	402.5	39.00	6.0	0.0500	210	355.0	210	355.0	138.4	0.20	0.30	0.00	2.00	1	0.28	233970
Borgelt et al. [20]	2024	320.0	14.0	219.0	20.00	402.5	39.00	6.0	0.0500	210	355.0	210	355.0	116.3	0.20	0.30	0.00	2.00	1	0.31	109500
Borgelt et al. [20]	2024	320.0	14.0	219.0	20.00	402.5	39.00	6.0	0.0500	210	355.0	210	355.0	138.8	0.20	0.30	0.00	2.00	1	0.23	355980
Borgelt et al. [20]	2024	320.0	14.0	219.0	20.00	402.5	39.00	6.0	0.0500	210	355.0	210	355.0	146.7	0.20	0.30	0.00	2.00	1	0.30	205994
Borgelt et al. [20]	2024	320.0	14.0	219.0	20.00	402.5	39.00	6.0	0.0500	210	355.0	210	355.0	142.1	0.20	0.30	0.00	2.00	1	0.25	311680
Borgelt et al. [20]	2024	320.0	14.0	219.0	20.00	402.5	39.00	6.0	0.0500	210	355.0	210	355.0	140.0	0.20	0.30	0.00	2.00	1	0.25	370753
Borgelt et al. [20]	2024	320.0	14.0	219.0	20.00	402.5	39.00	6.0	0.0500	210	355.0	210	355.0	140.0	0.20	0.30	0.00	2.00	1	0.38	58137
Borgelt et al. [20]	2024	320.0	14.0	219.0	20.00	402.5	39.00	6.0	0.0500	210	355.0	210	355.0	140.0	0.20	0.30	0.00	2.00	1	0.34	63681
Borgelt et al. [20]	2024	320.0	14.0	219.0	20.00	402.5	39.00	6.0	0.0500	210	355.0	210	355.0	140.0	0.20	0.30	0.00	2.00	1	0.44	28661
Borgelt et al. [20]	2024	320.0	14.0	219.0	20.00	402.5	39.00	6.0	0.0500	210	355.0	210	355.0	140.0	0.20	0.30	0.00	2.00	1	0.41	44442
Schaumann et al. [44]	2015	144.3	8.3	60.0	8.25	90.0	22.50	2.5	0.0556	210	355.0	210	355.0	90.0	0.18	0.30	0.00	0.30	1	0.50	493120
Schaumann et al. [44]	2015	144.3	8.3	60.0	8.25	90.0	22.50	2.5	0.0556	210	355.0	210	355.0	90.0	0.18	0.30	0.00	1.00	1	0.50	94231
Schaumann et al. [44]	2015	144.3	8.3	60.0	8.25	90.0	22.50	2.5	0.0556	210	355.0	210	355.0	140.0	0.20	0.30	0.00	2.00	1	0.50	65325
Schaumann et al. [44]	2015	144.3	8.3	60.0	8.25	90.0	22.50	2.5	0.0556	210	355.0	210	355.0	90.0	0.18	0.30	0.00	2.00	1	0.50	173238
Schaumann et al. [44]	2015	144.3	8.3	60.0	8.25	90.0	22.50	2.5	0.0556	210	355.0	210	355.0	90.0	0.18	0.30	0.00	5.00	1	0.50	48266
Schaumann et al. [44]	2015	144.3	8.3	60.0	8.25	90.0	22.50	2.5	0.0556	210	355.0	210	355.0	90.0	0.18	0.30	0.00	10.00	1	0.50	36719
Schaumann et al. [45]	2015	144.3	8.3	60.0	8.25	90.0	22.50	2.5	0.0556	210	355.0	210	355.0	140.0	0.20	0.30	0.00	1.00	1	0.50	91716
Schaumann et al. [45]	2015	144.3	8.3	60.0	8.25	90.0	22.50	2.5	0.0556	210	355.0	210	355.0	140.0	0.20	0.30	0.00	5.00	1	0.50	41789
Ingebrigtsen et al. [46]	1990	406.0	12.6	353.8	13.70	714.0	13.50	4.4	0.0065	200	240.0	200	240.0	40.1	0.20	0.30	94.24	1.00	0	0.85	345699
Ingebrigtsen et al. [46]	1990	406.0	12.8	357.0	13.30	714.0	11.70	4.4	0.0065	200	240.0	200	240.0	42.9	0.20	0.30	24.74	1.00	0	0.93	3950

Table A.1: (continued)

Source	Year	D_s (mm)	t_s (mm)	D_p (mm)	t_p (mm)	L_g (mm)	t_g (mm)	w (mm)	h/s	E_s (GPa)	$\sigma_{\mathrm{Y\_s}}$ (MPa)	E_p (GPa)	$\sigma_{\mathrm{Y\_p}}$ (MPa)	UCS_g (MPa)	v_g	v_s	P_min (kN)	f	env	$P_\mathrm{max}/P_\mathrm{static}$	N
Ingebrigtsen et al. [46]	1990	406.5	12.8	354.0	13.90	714.0	13.45	4.2	0.0062	200	240.0	200	240.0	44.1	0.20	0.30	50.34	1.00	0	0.83	56
Ingebrigtsen et al. [46]	1990	407.3	13.3	354.3	13.00	714.0	13.20	4.5	0.0066	200	240.0	200	240.0	43.8	0.20	0.30	-636.25	1.00	0	0.74	79
Ingebrigtsen et al. [46]	1990	407.5	13.5	354.5	12.80	714.0	13.00	4.5	0.0066	200	240.0	200	240.0	43.1	0.20	0.30	-651.30	1.00	0	0.77	63
Ingebrigtsen et al. [46]	1990	406.5	12.7	355.7	13.00	714.0	12.70	4.4	0.0065	200	240.0	200	240.0	43.4	0.20	0.30	-682.02	1.00	0	0.80	96
Ingebrigtsen et al. [46]	1990	405.5	13.6	355.5	12.50	714.0	11.40	4.5	0.0066	200	240.0	200	240.0	46.1	0.20	0.30	-1151.97	1.00	0	0.85	250
Ingebrigtsen et al. [46]	1990	406.0	13.5	356.0	13.80	714.0	11.50	4.6	0.0068	200	240.0	200	240.0	38.5	0.20	0.30	-1126.02	1.00	0	0.96	250
Ingebrigtsen et al. [46]	1990	406.8	13.4	354.8	14.10	714.0	12.60	3.8	0.0056	200	240.0	200	240.0	42.3	0.20	0.30	-1222.98	1.00	0	0.83	96
Ingebrigtsen et al. [46]	1990	409.1	12.9	356.1	13.40	714.0	13.60	4.5	0.0066	200	240.0	200	240.0	45.9	0.20	0.30	709.29	1.00	0	0.89	1050
Ingebrigtsen et al. [46]	1990	408.7	13.4	356.3	14.00	714.0	12.80	4.5	0.0066	200	240.0	200	240.0	45.8	0.20	0.30	-1842.45	1.00	0	0.73	20
Ingebrigtsen et al. [46]	1990	409.0	13.2	357.7	13.00	714.0	12.45	4.5	0.0066	200	240.0	200	240.0	46.6	0.20	0.30	-1992.72	1.00	0	0.76	5
Ingebrigtsen et al. [46]	1990	408.8	13.2	356.9	12.40	714.0	12.75	4.5	0.0066	200	240.0	200	240.0	46.9	0.20	0.30	-1704.30	1.00	0	0.65	12

References

[1] Gupta BK, Basu D. Offshore wind turbine monopile foundations: Design perspectives. Ocean Eng 2020;213:107514.

[2] Sah UK, Yang J. Importance of higher modes for dynamic soil structure interaction of monopile-supported offshore wind turbines. Earthq Eng Struct Dyn 2024;53(6):2006-2031.

[3] Bechtel AC. Fatigue behaviour of axially loaded grouted connections in jacket structures. Leibniz Universität Hannover; 2016.

[4] Raba A. Fatigue behaviour of submerged axially loaded grouted connections. Leibniz Universität Hannover; 2018.

[5] Billington CJ., Tebbett IE. The basis for new design formulae for grouted jacket to pile connections. Offshore Technology Conference 1980, Houston, USA.

[6] Boswell LF., D'Mello C. The fatigue strength of grouted repaired tubular members. Offshore Technology Conference 1986, Houston, USA.

[7] Harwood RG., Billington CJ., Buitrago J., Sele AB., Sharp JV. Grouted pile to sleeves connections: design provisions for the new ISO standard for offshore structures 1996, Proceedings of the 15th International Conference on Offshore Structures and Arctic Engineering, New York, USA.

[8] Etterdal B., Askheim D., Grigorian H. Strengthening of offshore steel components using high-strength grout: component testing and analytical methods 2001, Offshore Technology Conference, Houston, USA.

[9] Anders S. Betontechnologische Einflüsse auf das Tragverhalten von Grouted Joints. Leibniz Universität Hannover; 2008.

[10] Anders S, Lohaus L. Optimized high performance concrete in grouted connections. Taylor and Francis Group; 2008.

[11] Chen T, Wang X, Yuan G, Liu J. Fatigue bending test on grouted connections for monopile offshore. Mar Struct 2018;60:52-71.

[12] Schaumann P., Lochte-Holtgreven S., Eichstädt R., Camp T., McCann G. Numerical investigations on local degradation and vertical misalignments of grouted joints in monopile foundations 2013, Proceedings of the 23rd International Offshore and Polar Engineering Conference, Anchorage, AK, USA.

[13] Sørensen EV., Westhof L., Yde E., Serednicki A. Fatigue life of high performance grout for wind turbine grouted connection in wet or dry environment 2011, Poster presented at EWEA OFFSHORE 2011, Amsterdam, Netherland.

[14] Schaumann P, Raba A, Bechtel A. Fatigue behaviour of grouted connections at different ambient conditions and loading scenarios. Energy Procedia 2017;137:196-203.

[15] Dallyn P, El-Hamalawi A, Palmeri A, Knight R. Experimental investigation on the development of wear in grouted connections for offshore wind turbine generators. Eng Struct 2016;113:89-102.

[16] Johansen A, Solland G, Lervik A, Strande M, Nybø T. Testing of jacket pile sleeve grouted connections exposed to variable axial loads. Mar Struct 2018;58:254-277.

[17] DNV-ST-0126. Support Structures for Wind Turbines Standard. Høvik: DNV GL; 2018.

[18] ISO 19902. Petroleum and Natural Gas Industries-Fixed Steel Offshore Structures. Switzerland: International Organization for Standardization; 2007.

[19] Lee J, Lee K, Kim S, Kang YJ. Evaluation of fatigue strength of high-strength grouted connections subjected to unidirectionally reversible cyclic loading. Ocean Eng 2021;235:109384.

[20] Borgelt J, Possekel J, Schaumann P, Ghafoori E. Mechanisms of fatigue degradation process in axially loaded grouted connections under submerged conditions. Int J Fatigue 2024;189:108576.

[21] API RP 2A-WSD. Recommended Practice for Planning, Designing and Constructing Fixed Offshore Platforms-working Stress Design. American: American Petroleum Institute; 2007.

[22] DNVGL-RP-0419. Analysis of grouted connections using the finite element method. Høvik: DNV GL; 2016.

[23] Gu Z, Liu Y, Hughes DJ, Ye J, Hou X. A parametric study of adhesive bonded joints with composite material using black-box and grey-box machine learning methods: Deep neuron networks and genetic programming. Compos B: Eng 2021;217:108894.

[24] Ding X, Hou X, Xia M, Ismail Y, Ye J. Predictions of macroscopic mechanical properties and microscopic cracks of unidirectional fibre-reinforced polymer composites using deep neural network (DNN). Compos Struct 2022;302:116248.

[25] Ding X, Gu Z, Hou X, Xia M, Ismail Y, Ye J. Effects of defects on the transverse mechanical response of unidirectional fibre-reinforced polymers: DEM simulation and deep learning prediction. Compos Struct 2023;321:117301.

[26] Liu Q, Shi W, Chen Z. Fatigue life prediction for vibration isolation rubber based on parameter-optimized support vector machine model. Fatigue Fract Eng Mater Struct 2019;42(3):710-718.

[27] Wang Q, Yao G, Kong G, Wei L, Yu X, Zeng J, Ran C, Luo L. A data-driven model for predicting fatigue performance of high-strength steel wires based on optimized XGBOOST. Eng Fail Anal 2024;164:108710.

[28] Xiang KL, Xiang PY, Wu YP. Prediction of the fatigue life of natural rubber composites by artificial neural network approaches. Mater Des 2014;57:180-185.

[29] Jian Y, Hu P, Zhou Q, Zhang N, Cai D, Zhou G, Wang X. A novel bidirectional LSTM network model for very high cycle random fatigue performance of CFRP composite thin plates. Int J Fatigue 2025;190:108627.

[30] Nowell D, Nowell PW. A machine learning approach to the prediction of fretting fatigue life. Tribol Int 2020;141:105913.

[31] Durodola JF, Ramachandra S, Gerguri S, Fellows NA. Artificial neural network for random fatigue loading analysis including the effect of mean stress. Int J Fatigue 2018;111:321-332.

[32] Yao L, Wang J, Chuai M, Lomov SV, Carvelli V. Physics-informed machine learning for loading history dependent fatigue delamination of composite laminates. Composites Part A Applied Science & Manufacturing 2024;187:108474.

[33] Raissi M, Perdikaris P, Karniadakis GE. Physics-informed neural networks: A deep learning framework for solving forward and inverse problems involving nonlinear partial differential equations. J Comput Phys 2019;378:686-707.

[34] Urbán JF, Stefanou P, Pons JA. Unveiling the optimization process of physics informed neural networks: How accurate and competitive can PINNs be?. J Comput Phys 2025;523:113656.

[35] Wang H, Zhang J, Li B, Xuan F. Machine learning-based fatigue life prediction of laser powder bed fusion additively manufactured Hastelloy X via nondestructively detected defects. Int J Struct Integr 2025;16(1):104-126.

[36] Dang L, He X, Tang D, Xin H, Wu B. A fatigue life prediction framework of laser-directed energy deposition Ti-6Al-4V based on physics-informed neural network. Int J Struct Integr 2025;16(2):327-354.

[37] Meng D, Yang S, Yang H, Jesus AD, Correia J, Zhu SP. Intelligent-inspired framework for fatigue reliability evaluation of offshore wind turbine support structures under hybrid uncertainty. Ocean Eng 2024;307:118213.

[38] Li H, Zhang Z, Li T, Si X. A review on physics-informed data-driven remaining useful life prediction: Challenges and opportunities. Mech Syst Signal Pr 2024;209:111120.

[39] Liao H, Pan J, Su X, Sun X, Chen X. A path-dependent adaptive physics-informed neural network for multiaxial fatigue life prediction. Int J Fatigue 2025;193:108799.

[40] Zhai G, Spencer BF, Yan J. Coupled data/physics-driven framework for accurate and efficient structural response simulation. Eng Struct 2025;327:119636.

[41] Dong Y, Yang X, Chang D, Li Q. Predicting fatigue life of multi-defect materials using the fracture mechanics-based physics-informed neural network framework. Int J Fatigue 2025;190:108626.

[42] Hao W, Shi D, Yang X, Li N, Su S, Fan Y. Multi-mode fatigue life prediction using machine learning inspired by damage physics. Int J Mech Sci 2025;304:110723.

[43] Baktheer A, Aldakheel F. Physics-based machine learning for fatigue lifetime prediction under non-uniform loading scenarios. Comput Methods Appl Mech Engrg 2025;444:118116.

[44] Schaumann P., Raba A. Influence of the loading frequency on the fatigue performance of submerged small-scale grouted joints 2015, Proceedings of the 12th German Wind Energy Conference, Bremen, Germany.

[45] Schaumann P., Raba A. Systematic testing of the fatigue performance of submerged small-scale grouted joints 2015, International Conference on Offshore Mechanics and Arctic Engineering, Newfoundland, Canada.

[46] Ingebrigtsen T., Loset Ø., Nielsen SG. Fatigue design and overall safety of grouted pile sleeve connections 1990, Offshore Technology Conference, Houston, USA.

[47] El Kadi H. Modeling the mechanical behavior of fiber-reinforced polymeric composite materials using artificial neural networks—A review. Compos struct 2006;73(1):1-23.

[48] Baghaei KA, Hadigheh SA. Artificial neural network prediction of transverse modulus in humid conditions for randomly distributed unidirectional fibre reinforced composites: a micromechanics approach. Compos Struct 2024;337:118073.

[49] Mentges N, Dashtbozorg B, Mirkhalaf SM. A micromechanics-based artificial neural networks model for elastic properties of short fiber composites. Compos B: Eng 2021;213:108736.

[50] Lundberg SM, Lee SI. A unified approach to interpreting model predictions. Adv Neural Inf Process 2017;30.

[51] Lee JH, Won DH, Jeong YJ, Kim SK, Kang YJ. Interfacial shear behavior of a high-strength pile to sleeve grouted connection. Eng Struct 2017;151:704-723.